

Investigation of short-range structural order in $Zr_{69.5}Cu_{12}Ni_{11}Al_{7.5}$ and $Zr_{41.5}Ti_{41.5}Ni_{17}$ glasses, using X-ray absorption spectroscopy and *ab initio* molecular dynamics simulations

Debdutta Lahiri,^{a*} Surinder M. Sharma,^a Ashok K. Verma,^a B. Vishwanadh,^b G. K. Dey,^b Gerhard Schumacher,^c Tobias Scherb,^c Heinrich Rieseheimer,^d Uwe Reinholz,^d Martin Radtke^d and S. Banerjee^e

^aHigh Pressure and Synchrotron Radiation Physics Division, Bhabha Atomic Research Centre, Mumbai 400085, India, ^bMaterials Science Division, Bhabha Atomic Research Centre, Mumbai 400085, India, ^cHelmholtz-Zentrum Berlin für Materialien und Energie GmbH, Institut für Angewandte Materialforschung, Hahn-Meitner-Platz 1, D-14109 Berlin, Germany, ^dFederal Institute for Materials Research and Testing, Richard-Willstätter-Straße 11, Berlin 12489, Germany, and ^eBhabha Atomic Research Centre, Mumbai 400085, India.

*E-mail: debdutta.lahiri@gmail.com

Short-range order has been investigated in $Zr_{69.5}Cu_{12}Ni_{11}Al_{7.5}$ and $Zr_{41.5}Ti_{41.5}Ni_{17}$ metallic glasses using X-ray absorption spectroscopy and *ab initio* molecular dynamics simulations. While both of these alloys are good glass formers, there is a difference in their glass-forming abilities ($Zr_{41.5}Ti_{41.5}Ni_{17} > Zr_{69.5}Cu_{12}Ni_{11}Al_{7.5}$). This difference is explained by inciting the relative importance of strong chemical order, icosahedral content, cluster symmetry and configuration diversity.

Keywords: multi-component alloy; glass-forming ability; XAFS; local structure; AIMD simulation.

© 2014 International Union of Crystallography

1. Introduction

Growing interest in glass-forming alloys is inspired by their great technological promise (*e.g.* armour-penetrator, bio-medical implants, magnetic storage material, *etc.*) resulting from enhanced anti-corrosive and mechanical properties (Greer & Mathur, 2005; Greer, 1995; Ball, 2003). Since these enhanced properties hinge on amorphous/glassy structure, understanding the structure and its role in the glass-forming ability (GFA) of these alloys is important for their success (Yavari, 2006; Madden, 2005; Biazzo *et al.*, 2009; Cozzini & Ronchetti, 1996; He & Ma, 2001; Miracle, 2004; Sheng *et al.*, 2006*a,b*, 2008; Kelton *et al.*, 2003; Ma *et al.*, 2007, 2009; Mattern, 2009; Liu *et al.*, 2008; Saida *et al.*, 2000, 2007, 2008; Luo *et al.*, 2004; Zalewski *et al.*, 2009; Yang *et al.*, 2005, 2012; Saksl *et al.*, 2003; Long *et al.*, 2009; Herlach, 1994; Cahn, 1986; Inoue *et al.*, 1990; Inoue, 2000; Cheng *et al.*, 2008; Shi & Falk, 2006; Tanaka, 2005; Peng *et al.*, 2010; Li *et al.*, 2009; Takeuchi *et al.*, 2009; Greer, 1993).

Close-packed icosahedra, incompatible with translational symmetry, are the most widely recognized structural units of metallic glasses. As the number (n) of atomic components (X_n) of the alloy increases (*e.g.* multi-component alloy), the system becomes confused and disfavours any preferential structural order, a phenomenon called the ‘confusion prin-

ciple’ (Greer, 1993); instead, the structural configuration assumes distribution. Thus, multi-component systems, owing to their inherent disorder, are more inclined to be amorphous in character which promotes their GFA. Further composition-dependent modulations by chemical order, packing efficiency, *etc.* are the factors which determine the final structure of the system (Cheng *et al.*, 2009; Fujita *et al.*, 2009; Köster *et al.*, 1996; Lee *et al.*, 2008).

In this work we critically assess the role of short-range order (SRO), particularly the relative importance of chemical ordering, icosahedral content, cluster shape symmetry and configuration diversity, on relative GFA of two multi-component glasses, *viz.* $Zr_{69.5}Cu_{12}Ni_{11}Al_{7.5}$ ($n = 4$) and $Zr_{41.5}Ti_{41.5}Ni_{17}$ ($n = 3$) (Köster *et al.*, 1996; Lee *et al.*, 2008). While both these alloys are good glass formers and yield quasi-crystalline daughter phases, their GFA differ on a relative scale: $GFA = Zr_{41.5}Ti_{41.5}Ni_{17} \approx Zr_{69.5}Cu_{12}Ni_{11}Al_{7.5}$; $\delta(GFA) \geq 25\%$. For each alloy we derived site-resolved SRO for glassy and daughter phases of both the alloys, by employing X-ray absorption spectroscopy (XAS) (Prins & Koningsberger, 1987) and supporting with *ab initio* molecular dynamics (AIMD) simulations. To comprehend the extent of chemical ordering in these alloys we employed XANES (X-ray absorption near-edge structure). [XANES is the portion of XAS spectra within 30 eV of the absorption edge and sensitive

to oxidation state, coordination chemistry, orbital hybridization, *etc.* (Prins & Koningsberger, 1987).]

The X-ray absorption spectrum $\mu(E)$ of matter is modulated from the atomic absorption coefficient $\mu_0(E)$ by post-edge (E_0) oscillatory fine features, known as ‘X-ray absorption fine structure’ (XAFS). A photoelectron ejected from the excited atom ($BE = E_0$) is backscattered from the neighbouring atoms within radial distance ($R = 8\text{--}10 \text{ \AA}$). The interference, between backscattered and original photoelectron waves, gives rise to an oscillatory final-state vector in the absorption matrix. This is the origin of XAFS oscillations. The principle of XAFS is not based on long-range order, which makes it a unique probe for amorphous systems. Detailed structural information [*viz.* near-neighbour species (Z), their coordination (N), bond lengths (R) and mean square displacement (σ^2)] is derived from the Fourier transformation (FT) of XAFS oscillations. In the case of these multi-component alloys, several correlated XAFS variables could result in non-unique structural models. To select the final model unambiguously, we generated structural models from AIMD simu-

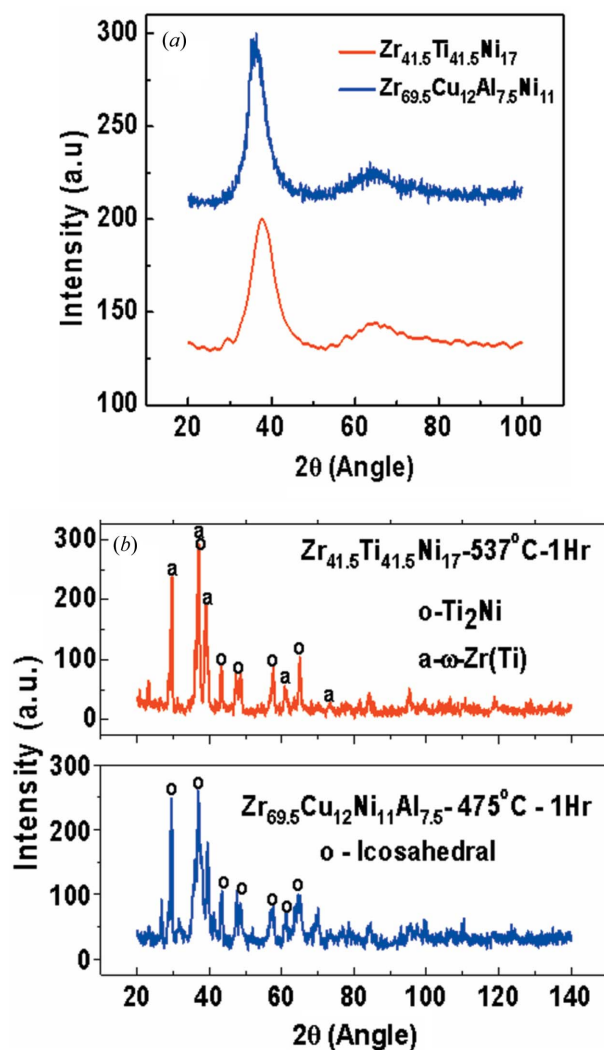


Figure 1
XRD of the (a) glassy and (b) annealed phases of $\text{Zr}_{41.5}\text{Ti}_{41.5}\text{Ni}_{17}$ and $\text{Zr}_{69.5}\text{Cu}_{12}\text{Ni}_{11}\text{Al}_{7.5}$.

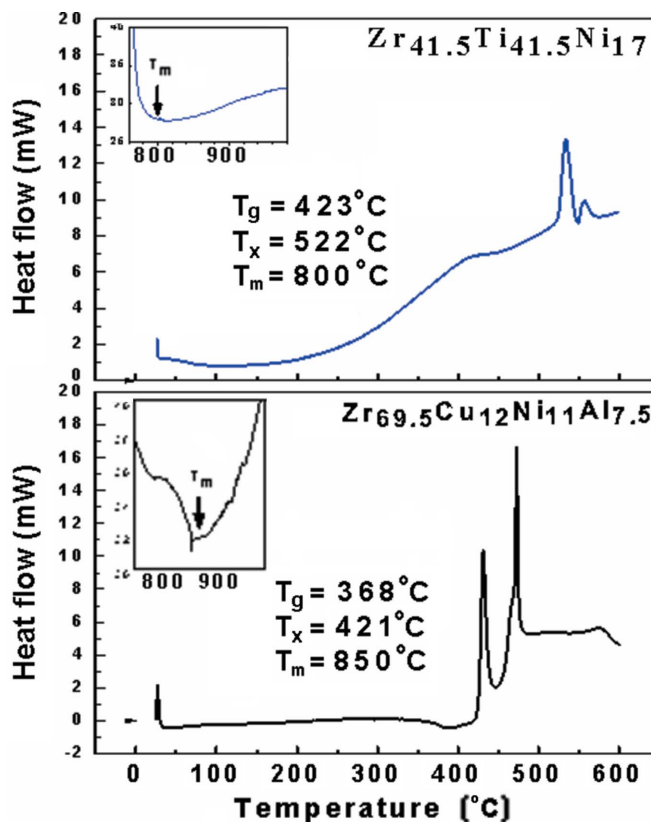


Figure 2
Differential scanning calorimetry results at low heating rate. Glass transition (T_g) and crystallization (T_x) temperatures are shown. Differential scanning calorimetry, at high heating rate, is shown in the inset. The melting temperature (T_m) is indicated.

lations independently and verified the consistency with XAFS results.

2. Experimental details

$\text{Zr}_{41.5}\text{Ti}_{41.5}\text{Ni}_{17}$ and $\text{Zr}_{69.5}\text{Cu}_{12}\text{Ni}_{11}\text{Al}_{7.5}$ alloys were prepared from pure Zr, Ti, Al, Cu and Ni by vacuum arc melting. The melt-spun ribbons (thickness = 20–30 μm ; width = 5 mm) were produced by rapid solidification of the melted alloy and amorphous character confirmed by X-ray diffraction (XRD) (Fig. 1a). Details of the synthesis method are provided elsewhere (Budhani *et al.*, 1982). From differential scanning calorimetry measurements (Fig. 2) we derived the relevant temperature points for calculating GFA, *viz.* (T_g , T_x , T_m) corresponding to glass transition, crystallization and melting, respectively (Table S1 of the supporting information¹). Different GFA parameterizations unanimously yield GFA: $\text{Zr}_{41.5}\text{Ti}_{41.5}\text{Ni}_{17} \approx 1.3 \times (\text{Zr}_{69.5}\text{Cu}_{12}\text{Ni}_{11}\text{Al}_{7.5})$ [$\delta(\text{GFA}) \geq 25\%$]. Some of these as-cast ribbons were annealed ($T > T_m$) for 1 h and quasi-crystalline daughter phases obtained (Fig. 1b). [In order to compare their GFA through casting diameter, both the alloys were suction casted into a 3 mm-diameter copper mould. Fig. S1(a) (see supporting information) shows the

¹ Supporting information for this paper is available from the IUCr electronic archives (Reference: HF5264).

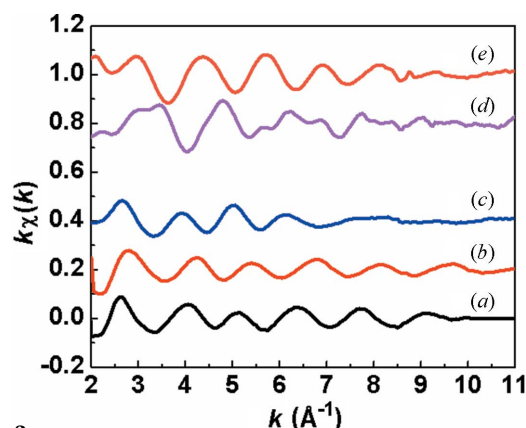


Figure 3
(a) Cu *K*-, (b) Ni *K*-, (c) Zr *K*-edges for $Zr_{69.5}Cu_{12}Ni_{11}Al_{7.5}$; (d) Ni *K*- and (e) Zr *K*-edges for $Zr_{41.5}Ti_{41.5}Ni_{17}$.

cylindrical rods of the as-cast Zr-based metallic glasses. To confirm the structure of the phases present in as-cast alloys, the samples were characterized by XRD. The XRD pattern of $Zr_{41.5}Ti_{41.5}Ni_{17}$ in Fig. S1(b) exhibits broad peaks, characteristic of amorphous structure. The XRD pattern of $Zr_{69.5}Cu_{12}Ni_{11}Al_{7.5}$ in Fig. S1(c) shows the presence of the diffraction peaks, characteristic of crystalline phases present in the sample. The presence of amorphous and crystalline phases in $Zr_{41.5}Ti_{41.5}Ni_{17}$ and $Zr_{69.5}Cu_{12}Ni_{11}Al_{7.5}$, respectively, confirms that the former has better GFA.]

XAFS spectra (*viz.* Cu, Ni and Zr *K*-edges on as-cast and annealed ribbon samples of each alloy) were recorded in transmission mode at BAMline, BESSY.² A Si (111) monochromator in conjunction with a harmonic rejection mirror was used to filter out the required wavelengths. Argon- and krypton-filled ionization chambers were used to monitor the incident and transmitted X-ray intensities, respectively. The data were processed using the *ATHENA* code³ and the resultant χ curves are shown in Fig. 3. The fast decay of XAFS oscillations beyond 10 \AA^{-1} is typical of amorphous materials. The data were fitted for the Fourier transform (FT) range ($\Delta k = 2.5\text{--}10 \text{ \AA}^{-1}$; $k^w = 1\text{--}3$) and *R*-range ($\Delta R \approx 1.5\text{--}3.0 \text{ \AA}^{-1}$), using the *FEFF8* and *FEFFIT* codes (Newville *et al.*, 1995). A good fit quality (*R*-factor < 0.01) was obtained in all cases (Newville *et al.*, 1995; Newville, 2001; Ravel & Newville, 2005).⁴

AIMD simulations were carried out using the finite-temperature local density functional theory, as implemented in the Vienna *ab initio* simulation package (VASP) (Kresse & Hafner, 1994; Kresse & Furthmüller, 1996; Fang *et al.*, 2009; Hui *et al.*, 2009). These calculations employ projector augmented wave (PAW) potentials along with a plane wave basis set. To obtain good convergence we used a plane wave energy cut-off of 450 eV. Brillouin zone integrations were carried out using the Γ point. The simulations were performed on a 200-atom cubic supercell with periodic boundary conditions. The initial configurations were prepared by randomly

placing the constituent atoms inside the cubic box at known experimental densities of 6.08 and 6.76 g cm^{-3} for ternary and quaternary systems, respectively. The simulations were carried out in a canonical ensemble (*NVT*) with a Nosé thermostat for temperature control and the equations of motion were solved with a time step of 3 fs. First the systems were melted at 2500 K, followed by a 6 ps equilibration period. Then these systems were quenched to 300 K at a rate of $\sim 12 \times 10^{13} \text{ K s}^{-1}$ (typical of *ab initio* simulations) (Hui *et al.*, 2009; Oji *et al.*, 2009), followed by a 6 ps equilibration period. It may be noted that the cooling rate in simulations is too fast compared with that during experimental quenching. While this may have influence on the development of medium-range order, short-range order is expected to be accurate (Oji *et al.*, 2009).

3. Results and discussion

3.1. Structure of the glassy phase

For each alloy, Fourier-transformed (FT) XAFS spectra of glassy and daughter (annealed) phases are shown in Fig. 4. The similarity between the spectra of glassy and respective daughter phases is consistent with a gradual crystallization process (discussed later).

It may be noted that the peaks at distances of less than 1.5 \AA are not real but result from the slight oscillatory character of the background fit polynomial. The background oscillation arises due to the limited *k*-range available ($2.5\text{--}10 \text{ \AA}^{-1}$). Following several background-fitting strategies (*e.g.* different *k* ranges, *k* weights, *R* ranges), the optimal background yields the observed peaks at low *R*. It may be clarified that the low-*R* limit ($\sim 1.5 \text{ \AA}$), for fitting the peak of interest ($\sim 1.5\text{--}3.0 \text{ \AA}$), is set such that the leakage from the background peak is negligible. Hence, the derived XAFS fit parameters are expected to be free of background-related artifacts.

3.1.1. $Zr_{69.5}Cu_{12}Ni_{11}Al_{7.5}$. AIMD simulations yielded partial distribution functions $g_{ik}(R)$ (*i*, *k* = Ni, Zr, Al, Cu) [Figs. 5(a) and 5(b)].⁵ The bond lengths (peak positions)⁶ are consistent with the literature (Kaban *et al.*, 2013; Takeuchi *et al.*, 2005). Out of these, R_{NiZr} (2.67 \AA) and R_{NiAl} (2.47 \AA) are significantly ($\sim 10\%$) shortened from their sum-of-atomic radii distances, *viz.* R_{Ni+Zr} (2.96 \AA) and R_{Ni+Al} (2.76 \AA), respectively. [Atomic radii were directly obtained from the respective homo-nuclear bond distances: R_{Cu} (1.25 \AA) \rightarrow R_{Al} (1.37 \AA) \rightarrow R_{Ni} (1.39 \AA) \rightarrow R_{Zr} (1.57 \AA)]. This indicates the existence of Ni–Al and Ni–Zr chemical interactions (Pilarczyk, 2013) in the system (discussed later).

The partial pair coordination (N_{ik}) and total coordination number (CN) around each site ($N_i = \sum_k N_{ik}$) are obtained from the region within the first minima ($R_c \approx 4 \text{ \AA}$). The average CN around each site is thus obtained: $N_{Cu} \approx 10$; $N_{Al} \approx 12$; $N_{Ni} \approx 11$; $N_{Zr} \approx 13$. The shift in CN is consistent with the solute–solvent atomic size ratio (R^*) (Sheng *et al.*, 2006a,b; Miracle *et al.*, 2006). The ensemble-averaged CN = 12.5 ($= \sum_i \rho_i N_i$, where ρ_i is the stoichiometric fraction).

² http://www.helmholtz-berlin.de/pubbin/igama_output?modus=einzel&sprache=en&gid=1625&typoid=35512.

³ <http://cars9.uchicago.edu/~ravel/software/doc/Athena/html/athena.pdf>.

⁴ <http://cars.uchicago.edu/~newville/feffit/feffit.pdf>.

⁵ $g_{Al}(r)$; $g_{Cu}(r)$ are not shown.

⁶ AIMD bond lengths concur with XAFS bond lengths in Table 1.

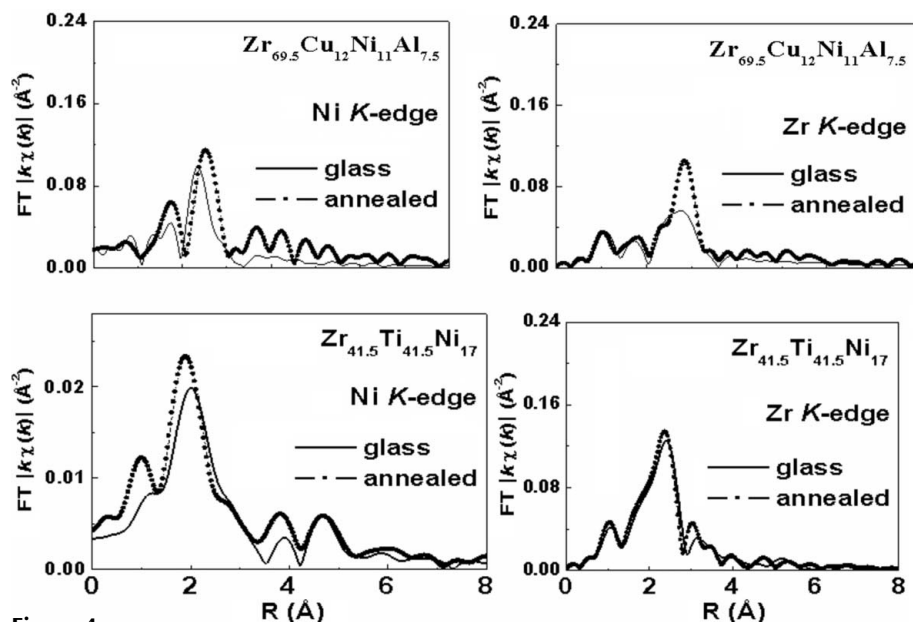


Figure 4
XAFS data for the glasses before and after annealing.

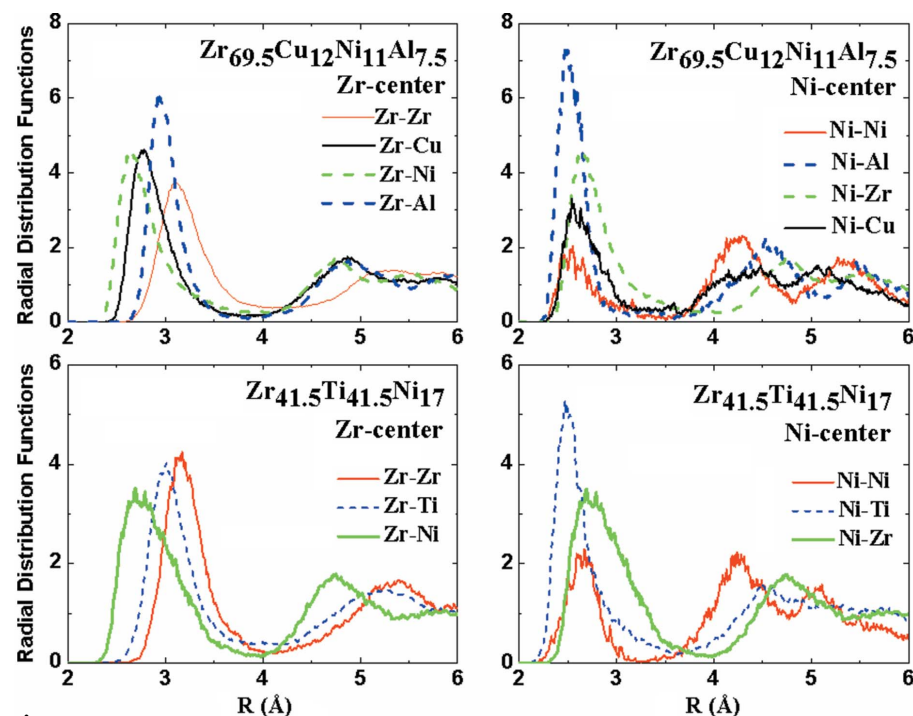


Figure 5
AIMD simulations for $\text{Zr}_{69.5}\text{Cu}_{12}\text{Ni}_{11}\text{Al}_{7.5}$ and $\text{Zr}_{41.5}\text{Ti}_{41.5}\text{Ni}_{17}$ around the Zr and Ni centres.

As mentioned, the above are only average results; in reality the ensemble consists of a distribution of cluster configurations and the nature of the distribution has important implications for GFA. In Fig. 6(a) we show the site-resolved CN distribution $(N_j, f_j)_i$ for this glass [$i = (\text{Ni}, \text{Zr}, \text{Al}, \text{Cu})$; $N_j = 8-16$; $f_j =$ frequency of clusters]; the main peak position $(N_j)_i$ shifts in agreement with R_j^* . From Fig. 6(a) we generated $\sum_i \rho_i(N_j, f_j)_i$, i.e. the distribution (N_j, F_j) of the entire ensemble, in Fig. 6(b). We observe that clusters with $N = 12-14$ are the most dominant ($\sum_{j=12}^{14} F_j = 75\%$; $F_{12,13,14} \sim 25\%$) in the ensemble, comparable with reported multi-component

glasses (Yang *et al.*, 2013; Hui *et al.*, 2009; Fang *et al.*, 2009; Fujita *et al.*, 2009; Cheng *et al.*, 2009). [For each CN, clusters of slightly varying geometry exist.] With such a narrow CN distribution ($N = 12-14$) and small variation in cluster volume (first shell radius ≈ 2.6 Å) and geometry, the configuration primarily resembles ‘quasi-equivalent clusters’, similar to that observed for good glass formers (Sheng *et al.*, 2006a,b, 2008). A secondary cluster domain with $N = 10$ ($F_{10} = 12\%$) coexists in the ensemble (around the smaller centres), adding non-uniformity to the configuration (discussed later).

Independent XAFS data fitting yielded nearest-neighbour bond lengths (Table 1) consistent with AIMD results. (Fits are compared with data in Fig. 7.) Despite multiple components, analysis was simplified by (i) ignoring the (negligible) contribution of Al due to its low stoichiometric fraction and back-scattering factor, and (ii) treating Ni and Cu scattering paths equivalently owing to their indistinguishable backscattering factors and similar bond lengths (Fig. 5). [$R_{\text{Ni-Ni}} = R_{\text{Ni-Cu}} = 2.6$ Å validates this assumption at the Ni K-edge. $|R_{\text{Zr-Cu}} - R_{\text{Zr-Ni}}| \approx 0.05$ Å is negligible; any attempt to separately fit these paths (Zr K-edge) was redundant and resulted in a large error bar. Thus, assumption (ii) is justified for the Zr K-edge as well.]

Following these assumptions, XAFS analysis is simplified to fitting two scattering paths (Ni, Zr) at each edge. To reduce further uncertainties in the (Ni, Zr) bond parameters, we simultaneously fitted the (Ni, Zr)-edge data with the common variable $(R_{\text{Ni-Zr}}, \sigma_{\text{Ni-Zr}}^2)$. From the XAFS fit results in Table 1, we observe that the total coordination around each site is lower than the AIMD results, e.g.

$$N_{\text{Ni}}^{\text{XAFS}} (\approx 3) \ll N_{\text{Ni}}^{\text{AIMD}} (\approx 11),$$

$$N_{\text{Zr}}^{\text{XAFS}} (\approx 6) \ll N_{\text{Zr}}^{\text{AIMD}} (\approx 13).$$

These results did not improve even with the inclusion of higher cumulants (Prins & Koningsberger, 1987; Fukuhara *et al.*, 2010).⁷

⁷ The ‘thickness effect’ may be ruled out since we measured samples with various degrees of polish (also splat-cooled) and thickness. The low coordination from Zr K-edge XAFS, despite the latter’s insensitivity to the thickness problem (due to large absorption length), asserts that the observed low coordination is real.

Table 1
XAFS fit results.

Bond type	Phase	Bond length (Å)	XAFS coordination number ($N_{\text{Ni}}^{\text{XAFS}}\dagger$)	DWF (Å ²)	
$\text{Zr}_{69.5}\text{Ni}_{11}\text{Cu}_{12}\text{Al}_{7.5}$	Ni—(Ni+Cu)	Glassy	2.61 (8)	0.36 ± 0.05	0.006 ± 0.002
		Annealed	2.72 (6)	0.68 ± 0.08	0.005 ± 0.002
	Ni—Zr	Glassy	2.61 (1)	2.61 ± 0.08	0.011 ± 0.001
		Annealed	2.72 (1)	2.91 ± 0.2	0.007 ± 0.001
	Cu—Zr	Glassy	2.72 (1)	2.39 ± 0.2	0.010 ± 0.001
		Annealed	2.81 (1)	3.22 ± 0.19	0.004 ± 0.001
Zr—Zr	Glassy	3.07 (1)	6.51 ± 0.58	0.023 ± 0.002	
	Annealed	3.16 (1)	6.51 ± 0.37	0.012 ± 0.002	
$\text{Zr}_{41.5}\text{Ti}_{41.5}\text{Ni}_{17}$	Ni—Ti	Glassy	2.59 (1)	2.64 ± 0.17	0.018 ± 0.002
		Annealed	2.54 (4)	2.30 ± 0.24	0.015 ± 0.002
	Ni—Zr	Glassy	3.11 (2)	1.11 ± 0.24	0.007 ± 0.003
		Annealed	3.07 (5)	0.71 ± 0.35	0.004 ± 0.006
	Zr—Ti	Glassy	3.06 (1)	5.96 ± 0.33	0.013 ± 0.001
		Annealed	3.02 (2)	3.94 ± 0.25	0.007 ± 0.001
	Zr—Zr	Glassy	3.23 (1)	8.09 ± 0.84	0.028 ± 0.003
		Annealed	3.14 (2)	8.23 ± 0.98	0.027 ± 0.003

† $S_0^2 = 0.8\text{--}0.9$ from measurement of standards.

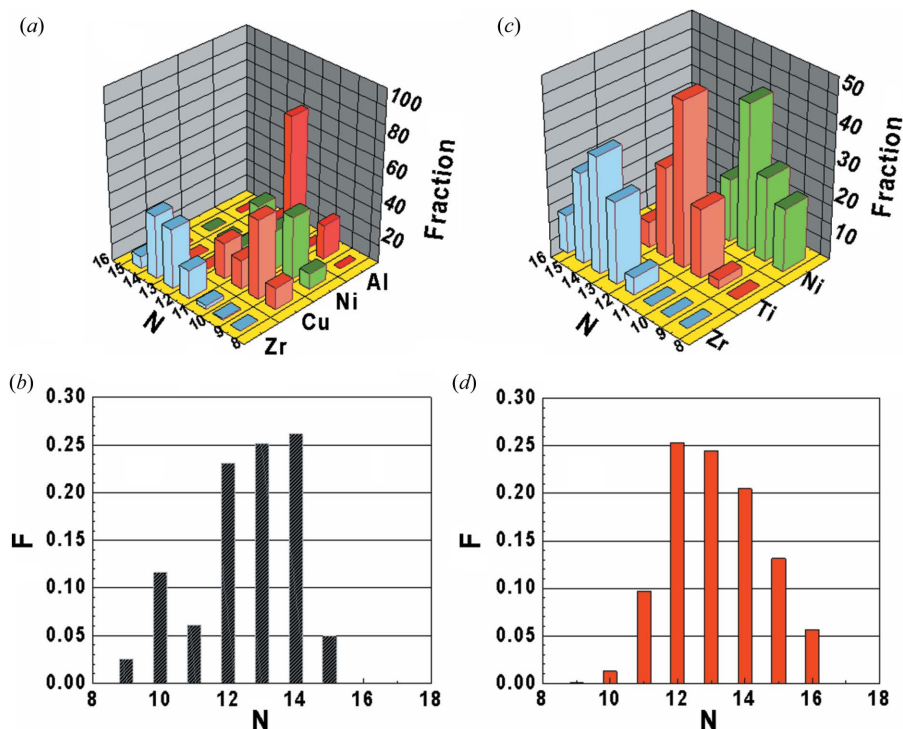


Figure 6
Site-resolved population distribution (%) of the nearest-neighbour coordination for (a) $\text{Zr}_{69.5}\text{Cu}_{12}\text{Ni}_{11}\text{Al}_{7.5}$ and (c) $\text{Zr}_{41.5}\text{Ti}_{41.5}\text{Ni}_{17}$. Ensemble-distribution for (b) $\text{Zr}_{69.5}\text{Cu}_{12}\text{Ni}_{11}\text{Al}_{7.5}$ and (d) $\text{Zr}_{41.5}\text{Ti}_{41.5}\text{Ni}_{17}$.

To reconcile these independently derived XAFS and AIMD coordination results, e.g. $N_{\text{Ni}}^{\text{XAFS}} (\approx 3) \ll N_{\text{Ni}}^{\text{AIMD}} (= 11)$, we consider the respective interpretation of coordination and its relevance to such highly disordered systems. In AIMD, N_i^{AIMD} is R_c -dependent (Sheng *et al.*, 2006a; Oji *et al.*, 2009). The positions of the first minima (R_c) are different for XAFS and AIMD [*viz.* $R_c^{\text{XAFS}} < R_c^{\text{AIMD}}$] due to a larger disorder in the

AIMD configuration and significant peak broadening. Reducing $R_c^{\text{AIMD}} = 4 \rightarrow 3 \text{ \AA}$ indeed reduces $N_{\text{Ni}}^{\text{AIMD}} \approx 11 \rightarrow 5 \approx N_{\text{Ni}}^{\text{XAFS}}$. On the other hand, $N_{\text{Ni}}^{\text{XAFS}}$ should be interpreted in an ‘effective’ sense (rather than absolute) for highly disordered systems (e.g. multi-site configuration). XAFS contributions from individual paths can be slightly out of phase with each other and reduce the net XAFS amplitude. This is reflected as reduced ($N_{\text{Ni}} \approx 3$) ‘effective’ XAFS coordination (Meyerheim *et al.*, 2012). Thus, $N_{\text{Ni}}^{\text{XAFS}} \approx 3$ in our case could well be consistent with $N_{\text{Ni}}^{\text{AIMD}} = 11$.

To reconcile the XAFS and AIMD results more conclusively, we constructed a Ni *K*-edge XAFS spectrum using the AIMD-generated atomic configuration. Scattering paths for the atoms were generated using *FEFF6*. With these paths and the ‘NOFIT’ option in the *feffit.inp* file, we simulated the normalized XAFS spectrum (with respect to the number of Ni atoms in the configuration). The simulated XAFS spectrum matches reasonably well with the experimental Ni *K*-edge XAFS spectrum (Fig. 8a). [The slight difference may be ignored considering that the AIMD-generated atomic configuration is highly disordered. This makes the theoretical XAFS spectrum highly sensitive to the exact atomic positions. The slight relative displacement of atoms (for test) resulted in reduction of the peak amplitude (de-phasing) or shift in the peak position.] By reproducing the experimental spectrum with $N_{\text{Ni}} = 11$ and large disorder, we could reconcile the AIMD and XAFS results and justify the low XAFS coordination ($N_{\text{Ni}} = 11 \rightarrow 3$).

To make our argument more conclusive, we actually fitted Ni *K*-edge XAFS using a theoretical AIMD distribution (Fig. 5b) as the basis for the fit and $R_c^{\text{AIMD}} = 3.2 \text{ \AA}$. [Since there is no XAFS feature beyond $R = 3 \text{ \AA}$ we have defined the XAFS fit range over $R = 1.5\text{--}3 \text{ \AA}$.

The contribution from the AIMD paths beyond 3.27 \AA is negligible.] A detailed description of the fit method is included in the supporting information. We obtained a good quality fit (shown in the inset of Fig. 8a). Our fit result, $R_{\text{NiZr}} = R_0 = 2.67 \text{ \AA}$; AIMD-based XAFS fit coordination, *viz.* $N_{\text{Ni}}^{\text{XAFS-AIMD}} = 4.5$, is now closer to our earlier model-independent XAFS fit result $N_{\text{Ni}}^{\text{XAFS}} = 3$ (*i.e.* $N_{\text{Ni}}^{\text{XAFS}} - N_{\text{Ni}}^{\text{AIMD-XAFS}} = -34\%$). This

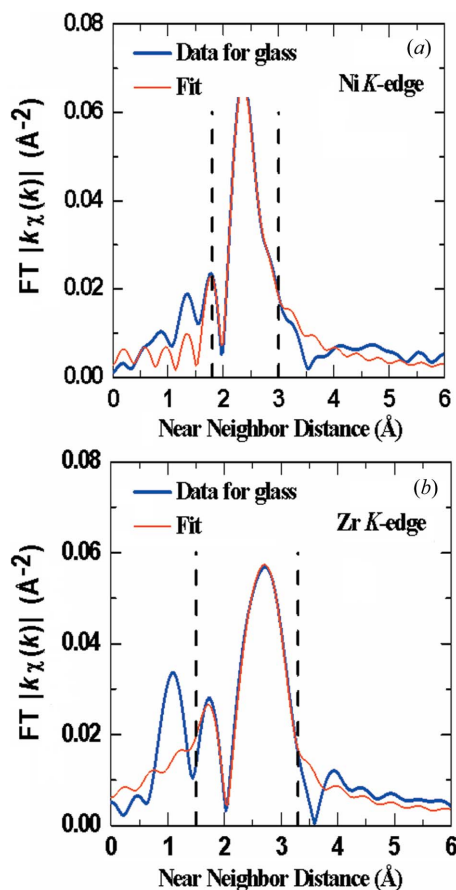


Figure 7
Comparison of fit with data for $\text{Zr}_{69.5}\text{Cu}_{12}\text{Ni}_{11}\text{Al}_{7.5}$ glass.

directly confirms our observation from AIMD: ‘ $R_c^{\text{AIMD}} = 4 \rightarrow 3 \text{ \AA}$ reduces $N_{\text{Ni}}^{\text{AIMD}} \approx 11 \rightarrow 5$ ’, and establishes an agreement between XAFS and AIMD coordination.

Additionally, we incite the sensitivity of the coordination to the degree of charge transfer between the central (Ni) and neighbour (Al, Ni/Cu, Zr) atoms. AIMD and XAFS both confirm Ni–Zr bond shortening (10%) from the sum-of-atomic-radii value, due to charge transfer (Ni–Al bond shortening is observed from AIMD). This suggests a change in the effective size of each ion (from its atomic size) which reduces the effective (centre: neighbour) atomic size ratio (R^*). Low N_{Ni} (as observed from XAFS) could be consistent with lower R^* (Miracle *et al.*, 2006), reflecting these ionic effects. The difference (>40%) between the AIMD and XAFS coordination has been reported earlier for glasses with strong chemical interaction (Liu *et al.*, 2012, 2014; Mansour *et al.*, 1994, 2002; Saksl *et al.*, 2005).

The conclusions for the Ni *K*-edge hold good for the Cu *K*-edge. However, the Zr *K*-edge results could not be validated unambiguously due to the larger disorder around the Zr sites. [Adding successive scattering paths progressively reduced the XAFS amplitude by de-phasing (Fig. 8*b*).]

3.1.2. $\text{Zr}_{41.5}\text{Ti}_{41.5}\text{Ni}_{17}$. AIMD simulations [Fig. 5(*c*) and 5(*d*)] yielded bond lengths consistent with the reported literature (Hennig *et al.*, 2003; Sadoc *et al.*, 2001, 2002; Mechler *et al.*, 2010*a*). The existence of a strong Ni–Ti interaction is

shown from the Ni–Ti bond shortening ($\sim 10\%$) from its sum-of-atomic-radii value [*i.e.* $R_{\text{NiTi}} (= 2.59 \text{ \AA}) < R_{\text{Ni}+\text{Ti}} (= 2.79 \text{ \AA})$]. The average CN around each site is consistent with R^* : $N_{\text{Ti}} \approx 12$; $N_{\text{Ni}} \approx 11$; $N_{\text{Zr}} \approx 14$ and ensemble averaged CN: $N = 13.1$.

Site-resolved and ensemble-averaged CN distributions are shown in Figs. 6(*c*) and 6(*d*), respectively. The site-resolved distribution in Fig. 6(*a*) demonstrates the R_i^* -dependent shift in peak position. In Fig. 6(*b*), the ensemble-averaged CN distribution extends over [$N = 11\text{--}15$]; out of these, clusters with CN = [12–14] emerge as the most dominant configuration ($\sum_{j=12}^{14} F_j = 70\%$). With such a narrow and continuous CN distribution, the ensemble configuration is consistent with the model of ‘quasi-equivalent clusters’.

Independent XAFS fitting results, listed in Table 1, yield similar bond lengths as AIMD. The first coordination shell around Ni is significantly distorted: (i) (Ti, Zr) atoms displace in opposite (\leftarrow , \rightarrow) directions (with respect to Ni), instead of converging at a common radial distance ($\Delta R = R_{\text{NiZr}} - R_{\text{NiTi}} = 0.5 \text{ \AA}$), signifying a strong Ni–Ti affinity and repulsive Ni–Zr interaction. (ii) $(N_{\text{Ni}}^{\text{Zr}}:N_{\text{Ni}}^{\text{Ti}}) \approx 0.4:1$, instead of 1.67:1 (Mechler

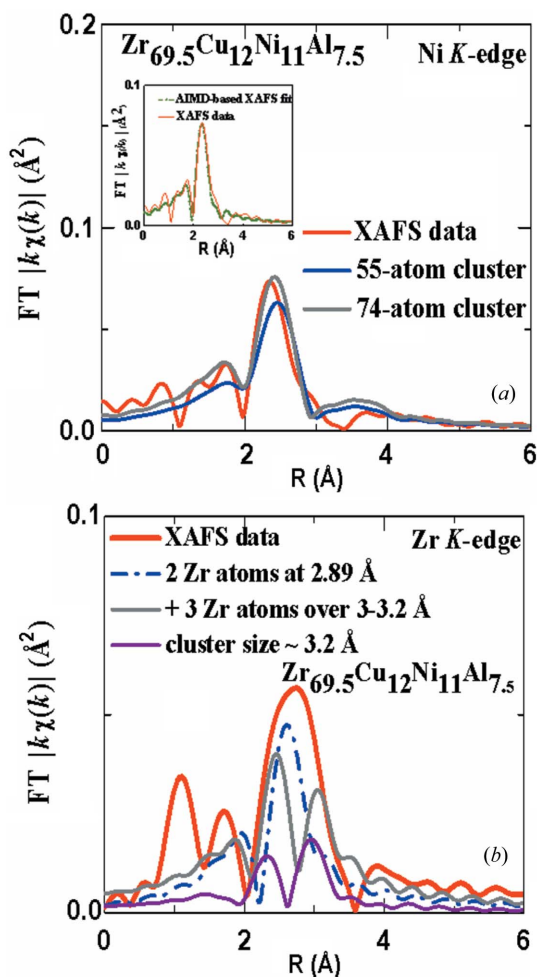


Figure 8
XAFS data compared with *FEFF* simulations generated from AIMD cluster configuration for $\text{Zr}_{69.5}\text{Cu}_{12}\text{Ni}_{11}\text{Al}_{7.5}$ around (a) Ni and (b) Zr. The AIMD-based fit is compared with XAFS data in the inset of (a).

et al., 2010b; Wang *et al.*, 2004). Reduced $N_{\text{Ni}}^{\text{Zr}}$ indicates several broken Ni–Zr bonds. Thus, both bond length and coordination features suggest the weakening of the Ni–Zr interaction by a much stronger Ni–Ti interaction (Antonowicz *et al.*, 2011).

3.1.3. Chemical order. To probe the extent of the chemical interaction in these glasses, we calculated the orbital projected density of states (PDOS) functions for each atomic species of the two alloys. From PDOS functions [Figs. 9(a) and 9(b)] it is obvious that both alloys are metallic as they have an appreciable amount of electronic density of states at the Fermi level. The main peaks of the Cu and Ni *d*-states lie a few electronvolts below the Fermi level. However, the *d*-states of Zr and Ti participate actively in the bonding as their main PDOS weight pass through the Fermi level. The *p*-states of Zr and Ti also contribute significantly to the bonding. The Ni *d*-states lie slightly deeper in $\text{Zr}_{69.5}\text{Cu}_{12}\text{Ni}_{11}\text{Al}_{7.5}$ but they show an appreciable overlap with different states of other atoms in both the systems [Figs. 9(a) and 9(b)]. From Fig. 9(b) the PDOS contribution of Ti clearly exceeds that of Zr by 50%, confirming the strong interaction of Ti. This is further supported by Ni *K*-edge XANES: comparison of the derivatives of the normalized spectra in Fig. 9(c) shows a significantly enhanced ($\times 2$) pre-edge feature (at 8332 eV) for $\text{Zr}_{41.5}\text{Ti}_{41.5}\text{Ni}_{17}$, compared with $\text{Zr}_{69.5}\text{Cu}_{12}\text{Ni}_{11}\text{Al}_{7.5}$ and Ni foil. X-ray absorption is dominated by the dipole transition rule ($\Delta l = \pm 1$), *e.g.* an $s \rightarrow p$ transition, which contributes to the main ($E > E_0$) peak of the XANES spectra. The pre-edge ($E < E_0$) peak results from transitions to hybridized orbitals ($s \rightarrow pd$) and is an indicator of *p*–*d* hybridization/charge transfer (Yamamoto, 2008). A strong ($\times 2$) pre-edge feature for $\text{Zr}_{41.5}\text{Ti}_{41.5}\text{Ni}_{17}$ (with respect to a 0– charge state in Ni foil) confirms a strong charge transfer to Ni, most likely from Ti. In comparison, the pre-edge of $\text{Zr}_{69.5}\text{Cu}_{12}\text{Ni}_{11}\text{Al}_{7.5}$ is only ($\sim 25\%$) developed relative to the Ni foil, suggesting a much lower charge transfer.

3.2. Structure of the annealed phases

The structural changes, upon annealing, demonstrate gradual relaxation towards respective equilibrium phases and improved ordering. The degree of structural evolution is bond-dependent and varies between the two alloys.

3.2.1. $\text{Zr}_{69.5}\text{Cu}_{12}\text{Ni}_{11}\text{Al}_{7.5}$. (i) Bond-lengths expand towards their respective values in $\text{NiZr}_2/\text{CuZr}_2$, *e.g.* $R_{\text{Ni-Zr}} = 2.61 \text{ \AA} \rightarrow 2.72 \text{ \AA}$ ($R_{\text{Ni-Zr}}|_{\text{NiZr}_2} = 2.77 \text{ \AA}$).⁸ (ii) Reduction of the Debye–Waller factor (DWF) ($|\Delta\sigma^2| = 30\text{--}60\%$) is consistent with the improved order in the annealed samples. (iii) Increased coordination ($\Delta N = 0\text{--}35\%$) represents retrieval of broken bonds in the process of atomic re-arrangement during ordering.

3.2.2. $\text{Zr}_{41.5}\text{Ti}_{41.5}\text{Ni}_{17}$. In this system, all bond lengths contract ($|\Delta R| \approx 0.04\text{--}0.1 \text{ \AA}$) towards their equilibrium (AIMD) values. Ordering, *viz.* $\Delta(N, \sigma^2)$, is negligible, considering error bars [except $\Delta(N, \sigma^2)_{\text{Zr-Ti}} > 20\%$].

⁸ The same is true for the other bonds.

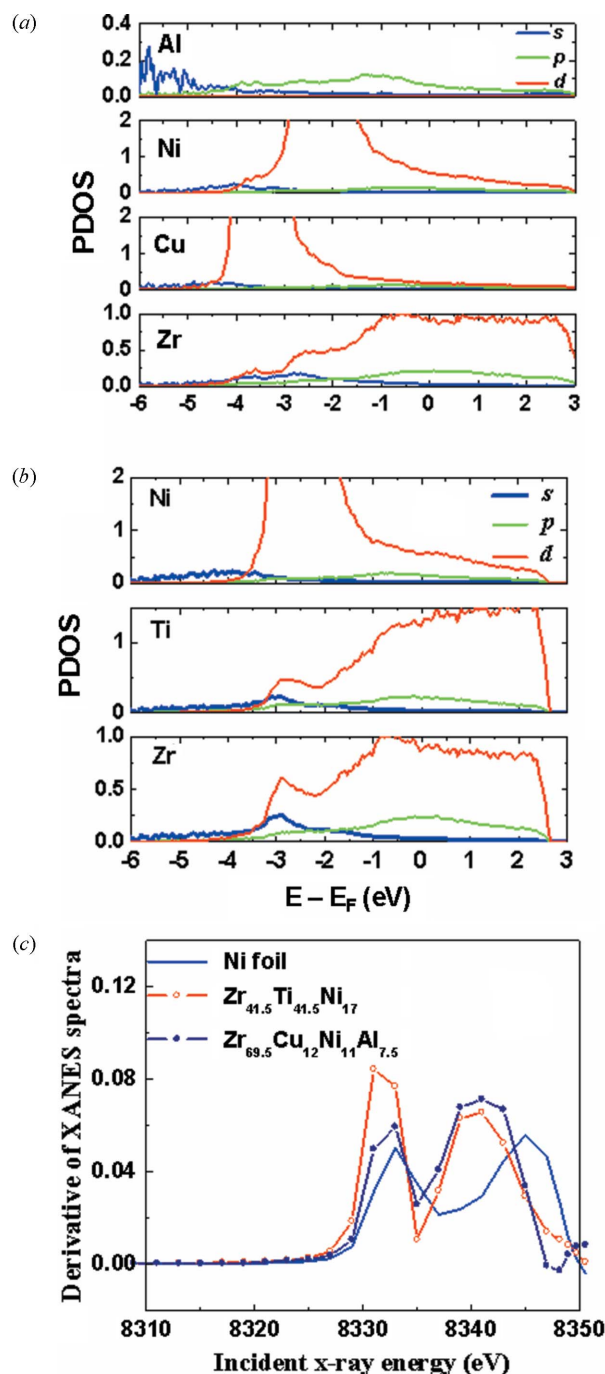


Figure 9 Atom projected electronic density of states PDOS (states $\text{eV}^{-1} \text{ atom}^{-1}$) of (a) $\text{Zr}_{69.5}\text{Cu}_{12}\text{Ni}_{11}\text{Al}_{7.5}$ and (b) $\text{Zr}_{41.5}\text{Ti}_{41.5}\text{Ni}_{17}$ glasses. (c) Derivative of XANES spectra for these glasses compared with Ni foil.

In both systems we consistently observe that the annealed structure is significantly far from the crystalline phases (*e.g.* NiZr_2)⁹, signifying the existence of a large crystallization barrier. It is likely that a strong chemical interaction (*viz.* Ni–Al, Ni–Zr, Ni–Ti) raises this barrier, restricts atomic mobility and arrests crystallization (Yang *et al.*, 2010; Pilarczyk, 2013).

⁹ NiZr_2 : $R_{\text{NiZr}} = 2.79 \text{ \AA}$ ($N = 8$); $R_{\text{ZrZr}} = 2.82\text{--}3.17 \text{ \AA}$ ($N = 3$); $R_{\text{ZrZr}} = 3.3\text{--}3.47 \text{ \AA}$ ($N = 8$).

3.3. Structure and glass-forming ability

Compiling all these results, we list the relevant (with respect to GFA) SRO parameters of $Zr_{69.5}Cu_{12}Ni_{11}Al_{7.5}$ and $Zr_{41.5}Ti_{41.5}Ni_{17}$. Both of these alloys are good glass formers, as shown from their thermal parameters (Table S1), quasi-crystalline daughter phases (Fig. 1*b*) and large crystallization barrier (Fig. 4). Consistently, the SRO of the two alloys is broadly similar ($\pm 5\%$) and comparable with the SRO parameters of reported good glass formers, *viz.* (i) ISRO content ($F_{12} \approx 25\%$), (ii) configuration model (= quasi-equivalent clusters), (iii) dominant cluster configuration ($N = 12\text{--}14$; $F \approx 70\text{--}75\%$), (iv) ensemble-averaged coordination ($N \approx 12$) and (v) strong chemical interaction [(Ni–Al, Ni–Zr); (Ni–Ti)], resulting in bond shortening. SRO parameters promote GFA by enhancing the packing efficiency and amorphous template; in parallel, strong chemical interaction suppresses their crystallization by raising the crystallization barrier and restricting atomic mobility.

To understand their relative GFA difference, *viz.* $Zr_{41.5}Ti_{41.5}Ni_{17} > Zr_{69.5}Cu_{12}Ni_{11}Al_{7.5}$ [$\delta(\text{GFA}) \geq 25\%$], we incite the importance of cluster shape non-uniformity and strength of chemical interaction:

(i) On a relative scale, the CN distribution of $Zr_{69.5}Cu_{12}Ni_{11}Al_{7.5}$ demonstrates the tendency for increased cluster shape non-uniformity by the presence of two domains, *viz.* $N = 12\text{--}14$ ($F \approx 75\%$), $N = 10$ ($F \approx 12\%$). The latter forms around smaller centres (*e.g.* Cu, Al); non-uniformity is thus a consequence of the large variance in the constituent atomic sizes of this alloy. In contrast, the CN distribution of $Zr_{41.5}Ti_{41.5}Ni_{17}$ is smooth. The correlation between good GFA and regular shape symmetry has been established in earlier work (Guo *et al.*, 2011; Xi *et al.*, 2007; Sha *et al.*, 2010). From this perspective, a smoother CN distribution of $Zr_{41.5}Ti_{41.5}Ni_{17}$ could have contributed towards its better GFA.

(ii) From our XANES results, it is clear that the chemical (Ni–Ti) interaction is significantly much stronger in $Zr_{41.5}Ti_{41.5}Ni_{17}$ involving a large degree of *p*–*d* hybridization: (100% *versus* 25%) in $Zr_{41.5}Ti_{41.5}Ni_{17}$ and $Zr_{69.5}Cu_{12}Ni_{11}Al_{7.5}$, respectively. Owing to this strong chemical interaction, atomic mobility is arrested and the crystallization barrier is significantly larger in $Zr_{41.5}Ti_{41.5}Ni_{17}$. This is shown from negligible ($\sim 0\%$) structural evolution (post-annealing). In comparison, the relatively relaxed chemical interaction in $Zr_{69.5}Cu_{12}Ni_{11}Al_{7.5}$ allows for ($\geq 30\%$) ordering.

4. Conclusion

With the help of XAFS measurements and AIMD simulations, we have attempted to obtain a structural understanding of the relative glass-forming-abilities of $Zr_{69.5}Cu_{12}Ni_{11}Al_{7.5}$ and $Zr_{41.5}Ti_{41.5}Ni_{17}$ ($Zr_{41.5}Ti_{41.5}Ni_{17} > Zr_{69.5}Cu_{12}Ni_{11}Al_{7.5}$). While both are good glass formers and have broadly similar short-range order, noticeable differences in cluster shape uniformity and strength of chemical interaction exist between the two systems. We show that these two factors play crucial roles in determining their relative glass-forming abilities. Glass

formation is more favoured for $Zr_{41.5}Ti_{41.5}Ni_{17}$ by smoother cluster distribution in the ensemble and a significantly stronger (Ni–Ti) chemical interaction; the former enhances amorphous packing efficiency and the latter increases the crystallization barrier. Thus, this work emphasizes the crucial role of these two factors on the glass-forming abilities of competitive and broadly similar systems.

DL would like to thank the Department of Science and Technology, Government of India, and Helmholtz Zentrum Berlin für Materialien und Energie, Berlin, Germany, for their support for the XAFS experiments.

References

- Antonowicz, J., Pietnoczka, A., Zalewski, W., Bacewicz, R., Stoica, M., Georgarakis, K. & Yavari, A. (2011). *J. Alloy. Compd.* **509**, S34–S37.
- Ball, P. (2003). *Nature (London)*, **421**, 783–784.
- Biazzo, I., Caltagirone, F., Parisi, G. & Zamponi, F. (2009). *Phys. Rev. Lett.* **102**, 195701.
- Budhani, R. C., Goel, T. C. & Chopra, K. L. (1982). *Bull. Mater. Sci.* **4**, 549–561.
- Cahn, R. W. (1986). *J. Vac. Sci. Technol. A*, **4**, 3071–3077.
- Cheng, Y. Q., Ma, E. & Sheng, H. W. (2009). *Phys. Rev. Lett.* **102**, 245501.
- Cheng, Y. Q., Sheng, H. W. & Ma, E. (2008). *Phys. Rev. B*, **78**, 014207.
- Cozzini, S. & Ronchetti, M. (1996). *Phys. Rev. B*, **53**, 12040–12049.
- Fang, H. Z., Hui, X., Chen, G. L. & Liu, Z. K. (2009). *Appl. Phys. Lett.* **94**, 091904.
- Fujita, T., Konno, K., Zhang, W., Kumar, V., Matsuura, M., Inoue, A., Sakurai, T. & Chen, M. W. (2009). *Phys. Rev. Lett.* **103**, 075502.
- Fukuhara, M., Fujima, N., Oji, H., Inoue, A. & Emura, S. (2010). *J. Alloy. Compd.* **497**, 182–187.
- Greer, A. L. (1993). *Nature (London)*, **366**, 303–304.
- Greer, A. L. (1995). *Science*, **267**, 1947–1953.
- Greer, A. L. & Mathur, N. (2005). *Nature (London)*, **437**, 1246–1247.
- Guo, G., Liang, Y., Huang, C. & Chen, D. (2011). *J. Mater. Res.* **26**, 2098–2102.
- He, J. H. & Ma, E. (2001). *Phys. Rev. B*, **64**, 144206.
- Hennig, R. G., Kelton, K. F., Carlsson, A. E. & Henley, C. L. (2003). *Phys. Rev. B*, **67**, 134202.
- Herlach, D. M. (1994). *Mater. Sci. Eng. Rep.* **12**, 177–272.
- Hui, X., Fang, H. Z., Chen, G. L., Shang, S. L., Wang, Y., Qin, J. Y. & Liu, Z. K. (2009). *Acta Mater.* **57**, 376–391.
- Inoue, A. (2000). *Acta Mater.* **48**, 279–306.
- Inoue, A., Zhang, T. & Masumoto, T. (1990). *Mater. Trans. JIM*, **31**, 177–183.
- Kaban, I., Jovári, P., Kokotin, V., Shuleshova, O., Beuneu, B., Saksl, K., Mattern, N., Eckert, J. & Greer, A. L. (2013). *Acta Mater.* **61**, 2509–2520.
- Kelton, K. F., Lee, G. W., Gangopadhyay, A. K., Hyers, R. W., Rathz, T. J., Rogers, J. R., Robinson, M. B. & Robinson, D. S. (2003). *Phys. Rev. Lett.* **90**, 195504.
- Köster, U., Meinhardt, J., Roos, S. & Liebertz, H. (1996). *Appl. Phys. Lett.* **69**, 179–181.
- Kresse, G. & Furthmüller, J. (1996). *J. Comput. Mater. Sci.* **6**, 15–50.
- Kresse, G. & Hafner, J. (1994). *J. Phys. Condens. Matter*, **6**, 8245–8257.
- Lee, G. W., Gangopadhyay, A. K., Hyers, R. W., Rathz, T. J., Rogers, J. R., Robinson, D. S., Goldman, A. I. & Kelton, K. F. (2008). *Phys. Rev. B*, **77**, 184102.
- Li, M., Wang, C. Z., Hao, S. G., Kramer, M. J. & Ho, K. M. (2009). *Phys. Rev. B*, **80**, 184201.
- Liu, X. J., Hui, X. D., Chen, G. L. & Sun, M. H. (2008). *Intermetallics*, **16**, 10–15.

- Liu, Y., Schumacher, G., Riesemeier, H. & Banhart, J. (2014). *J. Appl. Phys.* **115**, 203510.
- Liu, Y., Schumacher, G., Zizak, I., Erko, A. & Banhart, J. (2012). *Mater. Lett.* **70**, 171–173.
- Long, Z., Wei, H., Ding, Y., Zhang, P., Xie, G. & Inoue, A. (2009). *J. Alloy. Compd.* **475**, 207–219.
- Luo, W. K., Sheng, H. W., Alamgir, F. M., Bai, J. M., He, J. H. & Ma, E. (2004). *Phys. Rev. Lett.* **92**, 145502.
- Ma, D., Stoica, A. D., Wang, X. L., Lu, Z. P., Xu, M. & Kramer, M. (2009). *Phys. Rev. B*, **80**, 014202.
- Ma, D., Stoica, A. D., Yiang, L., Wang, X. L., Lu, Z. P. & Neuefeind, J. (2007). *Appl. Phys. Lett.* **90**, 211908.
- Madden, P. (2005). *Nature (London)*, **435**, 35–37.
- Mansour, A., Marcelli, A. & Cibin, G. (2002). *Phys. Rev. B*, **65**, 134207.
- Mansour, A., Wong, C. P. & Brizzolara, R. (1994). *Phys. Rev. B*, **50**, 12401–12412.
- Mattern, N. (2009). *J. Alloy. Compd.* **485**, 163–169.
- Mechler, S., Macht, M.-P., Schumacher, G., Zizak, I. & Wanderka, N. (2010b). *Phys. Rev. B*, **81**, 180101.
- Mechler, S., Schumacher, G., Koteski, V., Riesemeier, H., Schäfers, F. & Mahnke, H.-E. (2010a). *Appl. Phys. Lett.*, **97**, 041914.
- Meyerheim, H. L., Crozier, E. D., Gordon, R. A., Xiao, Q. F., Mohseni, K., Negulyaev, N. N., Stepanyuk, V. S. & Kirschner, J. (2012). *Phys. Rev. B*, **85**, 125405.
- Miracle, D. B. (2004). *Nat. Mater.* **3**, 697–702.
- Miracle, D. B., Lord, E. A. & Ranganathan, S. (2006). *Mater. Trans.* **47**, 1737–1742.
- Newville, M., Ravel, B., Haskel, D., Rehr, J. J., Stern, E. A. & Yacoby, Y. (1995). *Physica B*, **208–209**, 154–156.
- Newville, M. (2001). *J. Synchrotron Rad.* **8**, 96–100.
- Oji, H., Handa, K., Ide, J., Honma, T., Yamaura, S., Inoue, A., Umesaki, N., Emura, S. & Fukuhara, M. (2009). *J. Appl. Phys.* **105**, 113527.
- Peng, H. L., Li, M. Z., Wang, W. H., Wang, C.-Z. & Ho, K. M. (2010). *Appl. Phys. Lett.* **96**, 012901.
- Pilarczyk, W. (2013). *Arch. Mater. Sci. Eng.* **63**, 19–25.
- Prins, R. & Koningsberger, D. C. (1987). *X-ray Absorption: Principles, Applications, Techniques of EXAFS, SEXAFS and XANES*. New York: John Wiley and Sons.
- Ravel, B. & Newville, M. (2005). *J. Synchrotron Rad.* **12**, 537–541.
- Sadoc, A., Kim, J. Y. & Kelton, K. F. (2001). *Philos. Mag. A*, **81**, 2911–2924.
- Sadoc, A., Majzoub, E. H., Huett, V. T. & Kelton, K. F. (2002). *J. Phys. Condens. Mater.* **14**, 6413–6426.
- Saida, J., Matsushita, M. & Inoue, A. (2000). *Appl. Phys. Lett.* **77**, 73–75.
- Saida, J., Sanada, T., Sato, S., Imafuku, M. & Inoue, A. (2007). *Appl. Phys. Lett.* **91**, 111901.
- Saida, J., Sanada, T., Sato, S., Imafuku, M., Li, C. & Inoue, A. (2008). *Z. Kristallogr.* **223**, 726–730.
- Saksl, K., Jovari, P., Franz, H. & Jiang, J. Z. (2005). *J. Appl. Phys.* **97**, 113507.
- Saksl, K., Franz, H., Jovari, P., Klementiev, K., Welter, E. & Ehnes, A. (2003). *Appl. Phys. Lett.* **83**, 3924–3926.
- Sha, Z. D., Feng, Y. P. & Li, Y. (2010). *Appl. Phys. Lett.* **96**, 061903.
- Sheng, H. W., Cheng, Y. Q., Lee, P. L., Shastri, S. D. & Ma, E. (2008). *Acta Mater.* **56**, 6264–6272.
- Sheng, H. W., Luo, W. K., Alamgir, F. M., Bai, J. M. & Ma, E. (2006a). *Nature (London)*, **439**, 419–425.
- Sheng, H. W., Ma, E., Liu, H. Z. & Wen, J. (2006b). *Appl. Phys. Lett.* **88**, 171906.
- Shi, Y. & Falk, M. L. (2006). *Scr. Mater.* **54**, 381–386.
- Takeuchi, A., Nakano, S., Hasegawa, M., Soda, K., Sato, H., Mizutani, U., Itoh, K. & Fukunaga, T. (2005). *Mater. Trans.* **46**, 2791–2798.
- Takeuchi, A., Yubuta, K., Makino, A. & Inoue, A. (2009). *J. Alloy. Compd.* **483**, 102–106.
- Tanaka, H. (2005). *J. Non-Cryst. Solids*, **351**, 678–690.
- Wang, X., Qi, M., Thiel, P. A. & Dong, C. (2004). *Philos. Mag.* **84**, 825–834.
- Xi, X. K., Li, L. L., Zhang, B., Wang, W. H. & Wu, Y. (2007). *Phys. Rev. Lett.* **99**, 095501.
- Yamamoto, T. (2008). *X-ray Spectrom.* **37**, 572–584.
- Yang, L., Ge, T., Guo, G. Q., Huang, C. L., Meng, X. F., Wei, S. H., Chen, D. & Chen, L. Y. (2013). *Intermetallics*, **34**, 106–111.
- Yang, L., Guo, G. Q., Chen, L. Y., Huang, C. L., Ge, T., Chen, D., Liaw, P. K., Saksl, K., Ren, Y., Zeng, Q. S., LaQua, B., Chen, F. G. & Jiang, J. Z. (2012). *Phys. Rev. Lett.* **109**, 105502.
- Yang, L., Guo, G., Chen, L., Wei, S., Jiang, J. & Wang, X. (2010). *Scr. Mater.* **63**, 879–882.
- Yang, L., Jiang, J. Z., Liu, T., Hu, T. D. & Uruga, T. (2005). *Appl. Phys. Lett.* **87**, 061918.
- Yavari, A. R. (2006). *Nature (London)*, **439**, 405–406.
- Zalewski, W., Antonowicz, J., Bacewicz, R. & Latuch, J. (2009). *J. Alloy. Compd.* **468**, 40–46.